

# High-resolution X-ray imaging and spectroscopy of the core of NGC 4945 with *XMM-Newton* and *Chandra*

N. J. Schurch, T. P. Roberts & R. S. Warwick

*Department of Physics and Astronomy, University of Leicester, University Road, Leicester, LE1 7RH*

## ABSTRACT

We utilize the complimentary capabilities of *XMM-Newton* and *Chandra*, to conduct a detailed imaging and spectral study of the nearby galaxy NGC 4945 focussing on its nucleus and immediate surroundings (within  $\sim 1$  kpc of the nucleus). A complex morphology is revealed including a predominantly hard, but partially resolved, nuclear source plus a spectrally soft, conically shaped X-ray “plume”, which extends  $30''$  (500 pc) to the northwest. In NGC 4945 our direct view of the active galactic nucleus (AGN) is blocked below  $\sim 10$  keV by extremely heavy line-of-sight absorption and the observed X-ray spectrum is dominated by multi-temperature thermal emission associated with the nuclear starburst and the X-ray plume. Nevertheless the signature of the AGN is present in the form of a neutral Compton reflection component and a 6.4 keV fluorescent iron  $K\alpha$  line. We conjecture that the site of the continuum reprocessing is the far wall of a highly inclined molecular torus, a geometry which is consistent with the presence of  $\text{H}_2\text{O}$  megamaser emission in this source. The soft spectrum ( $\sim 0.6$  keV) and limb-brightened appearance of the X-ray plume suggest an interpretation in terms of a mass-loaded superwind emanating from the nuclear starburst.

**Key words:** galaxies: individual: NGC4945 – galaxies: Seyfert – X-rays: galaxies.

## 1 INTRODUCTION

NGC 4945 is a nearby edge-on ( $i \sim 78^\circ$ ; Ott, 1995) spiral galaxy (type SBcd or SABcd), believed to be a member of the Centaurus group (Hesser et al. 1984), at a distance of between 3.7 Mpc and 8.1 Mpc (here we use 3.7 Mpc; Mauersberger et al. 1996). Near infra-red observations have revealed the nuclear region of NGC 4945 to contain a powerful, yet visually obscured starburst region with a  $\sim 200$ pc ( $\sim 10''$ ) ring morphology (Moorwood et al. 1996) and a total infrared luminosity (8–1000  $\mu\text{m}$ ) of  $2.2 \times 10^{10} L_\odot$  (Spoon et al. 2000).

Although much of the central activity can be explained in terms of a nuclear starburst, the presence of an active galactic nucleus (AGN) in NGC 4945 has been confirmed by the detection of a luminous and variable hard X-ray source, coincident with the centre of the galaxy (Iwasawa et al. 1993; Guainazzi et al. 2000). NGC 4945 harbours the brightest known Seyfert 2 nucleus at 100 keV (Done et al. 1996), but extremely heavy obscuration cuts-off the direct AGN continuum at energies below  $\sim 10$  keV (Guainazzi et al. 2000; Madejski et al. 2000). The measured X-ray column density ( $\sim 4 \times 10^{24}$  atom  $\text{cm}^{-2}$ ) places it on the threshold of being a Compton-thick Seyfert 2. After correctly accounting for the effects of Compton scattering in the absorbing material (Matt et al. 1999), the inferred intrinsic X-ray (0.1–200 keV)

luminosity is  $\sim 1.8 \times 10^{43}$  erg  $\text{s}^{-1}$  (Guainazzi et al. 2000). The soft to medium energy X-ray spectrum of the nucleus is comprised of both thermal emission associated with a nuclear starburst and emission generated through the reprocessing of the AGN continuum emission (Guainazzi et al. 2000).

The dense clouds that envelope the nuclear region produce a rich variety of molecular lines (Curran et al. 2001) including  $\text{H}_2\text{O}$  megamaser emission, which requires an edge-on inner disk geometry (Greenhill, Moran & Hernstein 1997). The megamaser emission provides a tight constraint on the mass of the central black hole,  $M_{\text{BH}} \approx 1.4 \times 10^6 M_\odot$ , implying that the AGN is radiating at up to 60% of its Eddington luminosity.

Infrared and optical observations of NGC 4945 have also revealed the presence of a conical cavity, attributed to a starburst-driven superwind, protruding above the disk of the galaxy (Chen & Huang 1997; Moorwood et al. 1996). Despite heavy obscuration at optical wavelengths, extended line-emitting gas, co-spatial with the conical cavity, has been detected in outflow along the galaxy’s minor-axis and is attributed to the interaction between the superwind and the surrounding medium (Heckman, Armus & Miley 1990). The low spatial resolution of the current published data has mitigated against the detection of the superwind in X-rays, although Guainazzi et al. (2000) suggest that at least part of

the soft X-ray emission from NGC 4945 may originate in this component.

Here we present new *XMM-Newton* and *Chandra* X-ray observations of NGC 4945. The X-ray imaging reveals a complex morphology within the nuclear region of NGC 4945 and considerable emission associated with the disk of the galaxy, including at least 12 discrete X-ray sources. In this paper we will confine our attention to a detailed analysis of the nuclear region of NGC 4945; the remaining diffuse emission associated with the galactic disk and the off-nuclear point source population will be discussed in a separate paper (Roberts, Schurch & Warwick 2002; in preparation).

## 2 OBSERVATIONS AND DATA REDUCTION

### 2.1 The *XMM-Newton* Observation

NGC 4945 was observed with *XMM-Newton* during orbit 205 (2001, January 21) for  $\sim 24$  ks as part of the mission Guaranteed Time programme. The EPIC MOS and PN instruments were operated in full frame mode, with the medium filter, for the full duration of the observation. Detailed summaries of the *XMM-Newton* mission and instrumentation can be found in Jansen et al. (2001; and references therein). The raw data were processed with the public release version of the *XMM-Newton* Science Analysis System (SAS v 5.2) standard processing chains. After filtering for data flagged as bad, X-ray events corresponding to pattern 0-12 for the two MOS cameras (similar to grades 0-4 for *ASCA*) and pattern 0-4 for the PN camera (single and double pixel events only) were accepted. Investigation of the full-field count-rate revealed no significant background flaring episodes in the observation. The effective exposure times for the MOS and PN cameras were 22.2 ks and 19.2 ks respectively. Images, spectra and corresponding background information were extracted with the SAS task XMMSELECT.

### 2.2 The *Chandra* observation

The archival *Chandra* data were obtained from the UK mirror of the *Chandra* X-ray Center data archive, maintained by the Leicester Data Archive Service (LEDAS). The *Chandra* observation itself was performed on 2000 January 27/28, resulting in a total exposure of 50 ks, with the ACIS-S array at the prime focus. Our reduction and analysis of this dataset was performed using version 2.1 of the CIAO software, and incorporated many of the standard analysis procedures available online from [cxc.harvard.edu/ciao](http://cxc.harvard.edu/ciao). The data were initially filtered to remove all events outside the 0.3-10 keV energy range. The analysis of the full-field light-curve revealed the observation to be heavily contaminated by background flaring. The removal of all times for which the total detector count rate exceeded  $8 \text{ counts s}^{-1}$  was found to dramatically reduce the background in the S3 chip, leaving a GTI-corrected event-list containing 33.1 ks of “good” data.

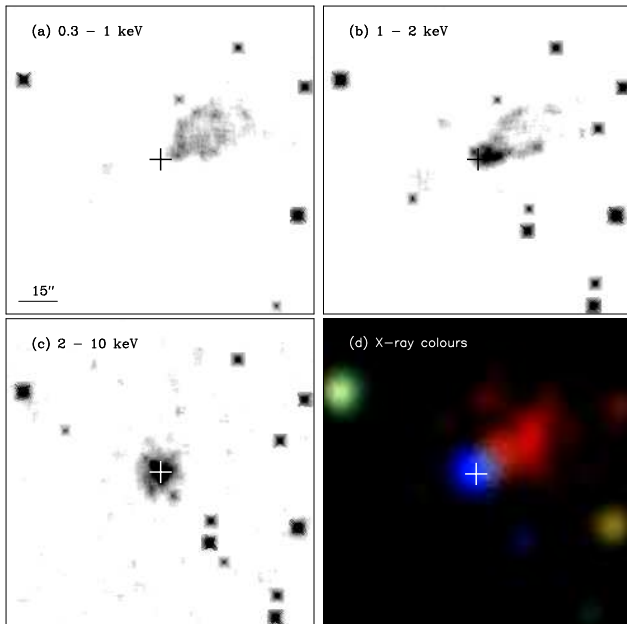


**Figure 1.** X-ray Images of the nuclear region of NGC 4945. *Panels a-c:* *Chandra* X-ray images corresponding to (a) the soft (0.3-1 keV) band; (b) the medium (1-2 keV) band and (c) the hard (2-10 keV) band. *Panel d:* *XMM-Newton* ‘X-ray colour’ image. Red, green and blue correspond to the soft, medium and hard X-ray bands defined above. All the images are  $2'$  on a side. The *Chandra* images have been smoothed with an adaptive ‘boxcar’ filter set to encompass  $\geq 10$  cts per box, or to have a half-width of 5 pixels. Non-adaptive, Gaussian smoothing ( $2''$  HWHM) was applied to the *XMM-Newton* image.

## 3 JOINT IMAGING WITH *CHANDRA* AND *XMM-NEWTON*

*XMM-Newton* and *Chandra* images were extracted for a  $2'$  square region centered on the nucleus of NGC 4945, revealing a wealth of detail including a predominantly hard nuclear source and a soft X-ray “plume” extending to the northwest of the nuclear source. Fig. 1: *Panels (a)-(c)*, show high spatial resolution energy-coded X-ray images from the *Chandra* ACIS detector, while Fig. 1: *Panel (d)* shows an ‘X-ray colour’ image from the co-added *XMM-Newton* EPIC cameras. Whereas the nuclear source appears point-like with *XMM-Newton*, the *Chandra* imaging partially resolves the emission centred on the active nucleus (Fig. 1: *Panel (c)*). The nuclear point source is revealed as an extremely hard source by both the *Chandra* hard band image and the *XMM-Newton* X-ray colour image. This spectral hardness is almost certainly due to heavy line-of-sight obscuration. Both *XMM-Newton* and *Chandra* clearly resolve the X-ray plume, establishing its orientation and extent along the minor axis of the galaxy ( $30'' = 500 \text{ pc}$ , NW) and also its intrinsic spectral softness (Fig. 1: *Panels (a),(b),(d)*). The medium band *Chandra* image reveals the X-ray plume to have a limb-brightened morphology, qualitatively similar to the morphology of the X-ray plume seen in NGC 253 (Strickland et al. 2000).

#### 4 JOINT SPECTROSCOPY WITH CHANDRA AND XMM-NEWTON

The high spatial resolution afforded by *Chandra* has allowed us to spatially resolve several of the major components that comprise the total X-ray emission from the nucleus of NGC 4945. However, the relatively low count-rate means the *Chandra* data cannot be used to place tight constraints on the spectral form of these components. Conversely, despite the greater count-rate, the lower angular resolution of *XMM-Newton* gives rise to some spatial confusion, which complicates the identification and spectral modelling of the components of the nuclear region. Fortunately, the *joint* analysis of the *Chandra* and *XMM-Newton* spectra removes many of these limitations.

We have adopted the following approach. We extract separate *Chandra* ACIS spectra for the AGN and the extended emission components and model these in turn. The identified spectral components are then combined into a composite spectral model which is fitted to the high signal-to-noise *XMM-Newton* EPIC spectra of the whole nuclear region. Finally, we consider combined fits to both the *Chandra* and *XMM-Newton* spectra. As expected, the latter provides the tightest constraints on the individual model parameters.

##### 4.1 The *Chandra* AGN spectrum

The spectrum of the point-like nuclear source (which we associate predominantly with the AGN in NGC 4945) was derived from the *Chandra* GTI-corrected event list using a circular extraction region of radius 6 pixels ( $3''$ ) centred on the peak of the X-ray emission, at  $13^{\text{h}}05^{\text{m}}27.5^{\text{s}}$ ,  $-49^{\circ}28'05''$  (J2000). The corresponding background spectrum was taken from a local source-free region. The resulting spectrum contains  $\sim 750$  counts (after background subtraction) with no significant signal below 1.5 keV.

In modelling the spectral form of the AGN we note that in several well studied Seyfert 2 galaxies, with column densities in excess of a few  $\times 10^{23}$  atoms  $\text{cm}^{-2}$ , it appears that a relatively unabsorbed Compton-reflection component dominates the 2–10 keV spectrum (e.g. Mrk 3 - Cappi et al. 1999, Sako et al. 2000; NGC 3281 - Vignali 2002). In such sources, the putative molecular torus may serve as a reprocessing site for the hard continuum generated by the AGN. Furthermore, for a highly inclined configuration, it is perfectly plausible that the geometry is such as to give a relatively clear view of the far-side wall of the torus. It follows that the observed Compton-reflection in Seyfert 2's may originated from this ‘‘far-wall’’ location.

We have tested this hypothesis for NGC 4945 by fitting the *Chandra* AGN spectrum with a model consisting of a very heavily absorbed power-law continuum, unabsorbed Compton reflection of the continuum (*pexcrav* model in XSPEC; Magdziarz & Zdziarski 1995) and an iron  $K\alpha$  fluorescence line at 6.4 keV. It turns out that the underlying hard continuum in this model has little impact even at 10 keV, implying neither the *Chandra* or *XMM-Newton* data can provide useful constraints on the parameters of the underlying continuum. Thus, the continuum characteristics (photon index,  $\Gamma$ , normalisation,  $K_{\text{pl}}$  and absorbing column,  $N_{\text{H}}$ ) were fixed at the values consistent with previous anal-

**Table 1.** Best-fit model parameters

| Parameter                   | Model A                            | Model B                            | Model C                            |          |
|-----------------------------|------------------------------------|------------------------------------|------------------------------------|----------|
| R                           | $0.029^{+0.003}_{-0.003}$          | -                                  | $0.016^{+0.002}_{-0.002}$          |          |
| $E_{\text{Fe}K\alpha}$      | $6.42^{+0.03}_{-0.03}$             | $6.4^a$                            | $6.396^{+0.005}_{-0.007}$          | <i>b</i> |
| $\sigma_{\text{Fe}K\alpha}$ | $0.11^{+0.04}_{-0.03}$             | $0^a$                              | $0.048^{+0.011}_{-0.013}$          | <i>b</i> |
| $K_{\text{Fe}K\alpha}$      | $2.2^{+0.4}_{-0.4} \times 10^{-5}$ | $0.7^{+0.2}_{-0.3} \times 10^{-5}$ | $2.4^{+0.2}_{-0.2} \times 10^{-5}$ | <i>c</i> |
| $N_{\text{H},1}$            | -                                  | $0.16^{a,d}$                       | $0.16^{a,d}$                       | <i>e</i> |
| kT <sub>1</sub>             | -                                  | $0.61^{+0.4}_{-0.9}$               | $0.60^{+0.03}_{-0.03}$             | <i>b</i> |
| K <sub>1</sub>              | -                                  | $2.7^{+0.4}_{-0.5} \times 10^{-5}$ | $2.6^{+0.3}_{-0.3} \times 10^{-5}$ | <i>f</i> |
| $N_{\text{H},2}$            | -                                  | $1.5^{+0.1}_{-0.3}$                | $1.8^{+0.1}_{-0.2}$                | <i>e</i> |
| kT <sub>2</sub>             | -                                  | $0.9^{+0.1}_{-0.1}$                | $0.87^{+0.08}_{-0.08}$             | <i>b</i> |
| K <sub>2</sub>              | -                                  | $5.1^{+1.0}_{-1.2} \times 10^{-4}$ | $6.5^{+0.8}_{-1.1} \times 10^{-4}$ | <i>f</i> |
| $N_{\text{H},3}$            | -                                  | $8.8^{+4.4}_{-3.5}$                | $12.1^{+1.1}_{-1.6}$               | <i>e</i> |
| kT <sub>3</sub>             | -                                  | $8.7^g$                            | $6.0^{+1.1}_{-0.8}$                | <i>b</i> |
| K <sub>3</sub>              | -                                  | $4.5^{+1.6}_{-1.2} \times 10^{-4}$ | $6.4^{+1.1}_{-0.9} \times 10^{-4}$ | <i>f</i> |
| $\chi^2/\text{d.o.f}$       | 32.3/29                            | 81/67                              | 290/269                            |          |

<sup>a</sup> Fixed parameter

<sup>c</sup> photons  $\text{s}^{-1} \text{cm}^{-2}$

<sup>e</sup>  $\times 10^{22} \text{cm}^{-2}$

<sup>g</sup> Unconstrained parameter

<sup>b</sup> keV

<sup>d</sup> Galactic column density

<sup>f</sup> photons  $\text{s}^{-1} \text{cm}^{-2} \text{keV}^{-1}$

yses of the high energy ( $>10$  keV) spectrum from both *Bep-poSAX* and *RXTE*. Specifically we take  $\Gamma=1.55$ ,  $K_{\text{pl}}=0.1$  photon  $\text{s}^{-1} \text{cm}^{-2} \text{keV}^{-1}$  and  $N_{\text{H}}=4 \times 10^{24} \text{cm}^{-2}$  (Guainazzi et al. 2000; Madejski et al. 2000). Also, the metal abundances were fixed at solar values, the high-energy spectral cutoff set at 200 keV and the relative reflection parameter (R) was initially constrained to lie in the range 0–2 with  $\cos(i)=0.5$ .

This model, with both the R parameter and the energy, intrinsic width and normalisation of the iron  $K\alpha$  line as free parameters, provides a good fit to the *Chandra* spectrum ( $\chi^2=32$  for 29 degrees of freedom; hereafter d.o.f) as illustrated in Fig. 2 (Upper Panel). The best-fit parameter values are given in Table 1 (Model A), where the quoted errors correspond to 90% confidence levels for one interesting parameter (*i.e.*  $\Delta\chi^2=2.71$ ). Modelling the *Chandra* spectrum in terms of a heavily absorbed direct continuum component (but with  $N_{\text{H}}$  an order of magnitude smaller than assumed above) plus a relatively unabsorbed scattered power-law component (*cf.* Guainazzi et al. 2000) yields a considerably worse fit ( $\chi^2=51.1$  for 29 d.o.f). The fit residuals (Fig. 2, Upper Panel) hint at some contamination of the *Chandra* AGN spectrum by a nuclear starburst component; our modelling of the composite spectrum takes account of this in a straightforward fashion (see §4.3).

##### 4.2 The *Chandra* starburst/X-ray plume spectrum

The *Chandra* spectrum of the extended nuclear X-ray emission encompassing the resolved nuclear starburst component and the X-ray plume structure was constructed using an elliptical extraction region centred on  $13^{\text{h}}05^{\text{m}}25.5^{\text{s}}$ ,  $-49^{\circ}27'54''$  (J2000), with the major axis aligned along a position angle of  $120^{\circ}$ , with a semi-major axis of  $30.5''$  and a semi-minor axis of  $13.4''$ . In this case, the AGN component was suppressed by excluding the region within  $3''$  of the nucleus. The resulting spectrum (after background subtraction using a local source-free region) contains  $\sim 1600$  counts. *Chandra* is capable of resolving the starburst region from the

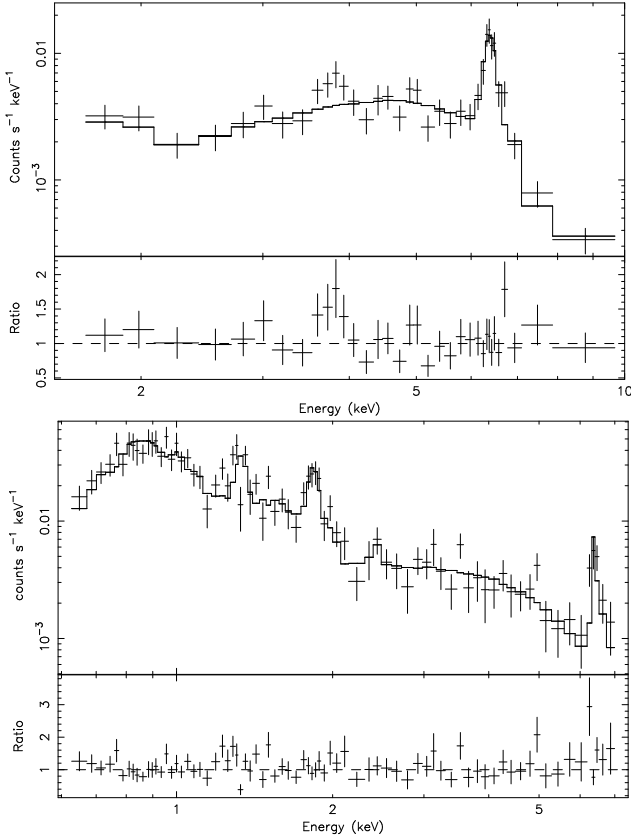


**Figure 2.** *Upper Panel:* *Chandra* ACIS-S spectrum of the AGN in NGC 4945. The spectral fit corresponds to Model A. The data/model residuals are plotted below the spectrum. *Lower Panel:* *Chandra* ACIS-S spectrum of the starburst/X-ray plume. The spectrum is fitted with Model B and the data/model residuals are again shown.

X-ray plume, but here we have chosen to utilize the better signal-to-noise of the combined spectrum. Taking as a lead the published results for the starburst and X-ray plume in NGC 253 (Pietsch et al. 2001), we have modelled the *Chandra* spectrum with three solar abundance thermal (*mekal*) components, each exhibiting different levels of absorption as well as different temperatures and normalisations.

This model yields a good fit to most of the observed spectral features, including the significant  $K\alpha$  emission from helium-like iron at 6.7 keV. However it does not account for the  $K\alpha$  emission from neutral iron observed at 6.4 keV. Analysis of the individual starburst and X-ray plume spectra confirm that both  $K\alpha$  emission lines originate entirely from the starburst region. We model the neutral iron  $K\alpha$  emission with the addition of an intrinsically narrow Gaussian line. A model comprising three thermal components plus an iron  $K\alpha$  line provides a reasonable fit to the data ( $\chi^2=89$  for 67 d.o.f, see Fig. 2; *Lower Panel*). The corresponding best-fit model parameters are listed in Table 1 (Model B).

### 4.3 Joint fitting of the composite *XMM-Newton* and *Chandra* spectra

The *XMM-Newton* spectra for the combined AGN, starburst and X-ray plume components were extracted using a  $30''$  radius circle centered on  $13^h 05^m 28^s$ ,  $-49^\circ 28' 01''$  (J2000). For

both the MOS and PN cameras, a corresponding background spectrum was extracted from a  $90''$  radius circle in a source free region of the same CCD. After background subtraction, each MOS spectrum contained  $\sim 1350$  counts compared to  $\sim 3500$  counts in the PN spectrum.

The *XMM-Newton* spectrum was analysed by combining the two models used in the description of the *Chandra* observations (Models A & B in §4.1 & §4.2). This composite model yields an excellent fit to the broadband *XMM-Newton* spectra ( $\chi^2=273.5$  for 268 d.o.f). However, an unphysical trade-off between the hottest thermal component and the Compton-reflection parameter result in a value of  $R$  which is inconsistent with the value found from the *Chandra* AGN spectrum alone (assuming that this component has not varied significantly over the one-year interval between the two observations, see §5.2). We have addressed this problem by performing *joint spectral fitting* of three spectral datasets, namely the *XMM-Newton* composite spectrum and the *Chandra* AGN and starburst/X-ray plume spectra. Only the Compton-reflection component, the iron line and the hottest thermal component were utilized in fitting the *Chandra* AGN spectrum, whilst only the three thermal components and the iron line were employed in relation to the *Chandra* starburst/X-ray plume spectrum. We also adapted the spectral model somewhat by fixing the absorption applied to the softest thermal component at the Galactic value and setting the absorption on the Compton-reflection component to be the same as that applied to the intermediate-temperature thermal component (*i.e.*  $N_{H,2}$ ).

Simultaneous fitting of the composite spectral model described above gives a good match to all three spectral datasets. The resulting best-fit to the *XMM-Newton* data is shown in Fig. 3; the corresponding parameters are given in Table 1 (Model C). The high signal-to-noise of the *XMM-Newton* spectra, relative to the *Chandra* spectra, leads to tighter constraints on all the parameters. The simultaneous fits highlight the important contribution of the highest temperature thermal (starburst) component to the 0.5-10 keV spectrum of NGC 4945. In this respect the joint spectral fitting is particularly valuable since the *Chandra* starburst/outflow spectrum has insufficient counts to put useful limits on the temperature of this component.

When data relating solely to the spatially-resolved X-ray plume are extracted (from both the *Chandra* and *XMM-Newton* datasets), the spectrum is found to be extremely soft with few counts above 2 keV. Spectral fitting using a single temperature *mekal* model, modified by Galactic absorption, gives a temperature and normalisation completely consistent with those of the softest thermal component in the composite spectral model (Model C), identifying this component with the X-ray plume emission. The two remaining thermal components are attributable to the nuclear starburst.

## 5 DISCUSSION

The components of the broadband spectrum of the extended nucleus of NGC 4945 are shown in Fig. 4. The Compton-reflection component makes a significant contribution between 5 and 10 keV, whereas at lower energies the spectrum is dominated by the thermal emission from the nuclear starburst and X-ray plume. The heavily absorbed AGN contin-

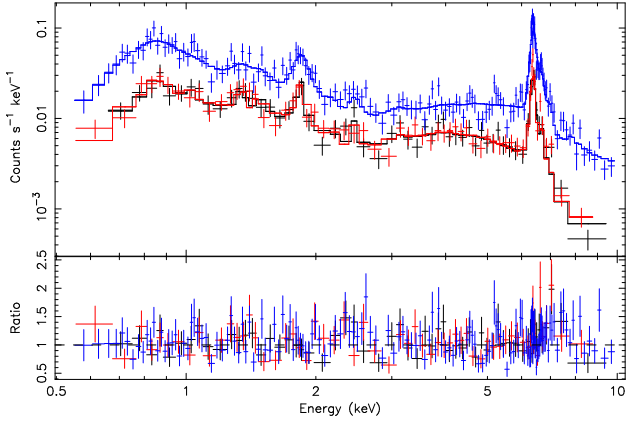


**Figure 3.** XMM-Newton EPIC MOS (black and red) and PN (blue) spectra of the extended nuclear region of NGC 4945. The spectra are fit with the composite model (Model C) and the data/model residuals are also shown.

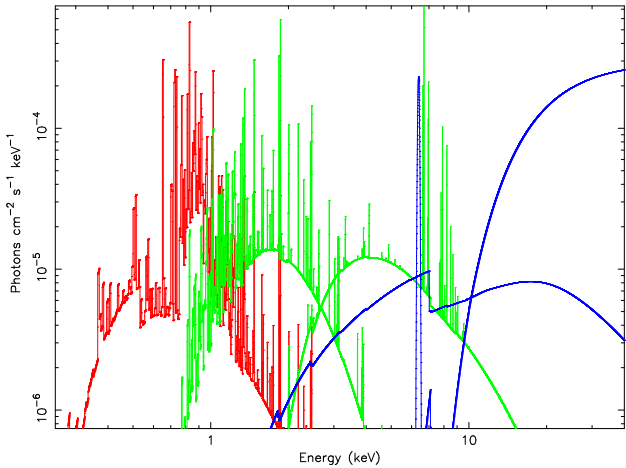


**Figure 4.** The broadband spectral model for the nucleus of NGC 4945. The component associated with the X-ray plume is shown in red, the starburst components in green and the AGN components in blue.

um only emerges above 10 keV. Strong  $K\alpha$  emission lines from neutral and helium-like iron are also present in the spectrum at 6.4 and 6.7 keV respectively.

### 5.1 The reprocessing of the AGN continuum

In the unified model proposed by Antonucci (1993), when an active nucleus is viewed at relative high inclination, the line of sight may intercept the surrounding molecular torus and hence be subject to significant obscuration. Previous observations testify to a near edge-on configuration of the inner disk in NGC 4945 (Greenhill, Moran & Hernstein 1997) and a very high line-of-sight column density to its active nucleus (Guainazzi et al. 2000; Madejski et al. 2000). Consistent with this picture, the analysis of the XMM-Newton and Chandra spectra of the nuclear region of NGC 4945 demonstrates that in the 0.5-10 keV range, there is only indirect evidence for the presence of the AGN (since the direct continuum is strongly cut-off below  $\sim 10$  keV).

One signature of the underlying AGN in NGC 4945 is

the Compton-reflection continuum which we attribute to re-processing off the far, inside wall of the molecular torus. In this scenario the ratio of the reflected to the direct continuum as embodied in Compton-reflection parameter,  $R$ , can be used to place a lower limit on the inclination angle of the torus, provided the geometrical configuration of the absorbing torus is known. In reality this is very uncertain, although the half-opening angle of tori are typically in the range  $20^\circ - 50^\circ$  (e.g. Wilson & Tsvetanov 1994). If we assume the geometry envisaged by Ghisellini, Haardt & Matt (1994), then our estimate of  $R = 0.016$  (based on the ‘average’ continuum given in Guainazzi et al. 2000) implies a near edge-on view of the torus. Alternatively a near edge-on but geometrically thin (half-angle  $\lesssim 10^\circ$ ) distribution of absorbing material located on parsec scales, as inferred by Madejski et al. (2000) on the basis of the hard X-ray variability seen in NGC 4945, is also consistent with a very low value for  $R$ .

The neutral iron  $K\alpha$  line is narrow and the nuclear component has an equivalent width of  $1.6 \pm 0.1$  keV with respect to the observed Compton-reflection continuum. This is fully consistent with the line and the reflected continuum originating at the same location, namely the visible part of the torus wall (e.g. Matt, Brandt & Fabian 1996). There is also a 30% contribution to the neutral iron  $K\alpha$  emission from the extended nuclear starburst region, implying that cool material in the environment of the starburst is also exposed to the AGN continuum flux.

Although the hard continuum emanating from the Seyfert 2 nucleus of NGC 4945 is known to be variable on timescales as short as  $\sim 10^4$ s (Guainazzi et al. 2000), no significant variability is detected in either the Chandra or XMM-Newton observations, nor is it evident from the joint spectral fits (the time interval between the two sets of observations being 12 months). This tallies with the location of the continuum reprocessing, namely the torus wall, lying at a distance in excess of a light year from the nuclear continuum source. (The apparent discrepancy between the Chandra-only and the joint-fit estimates of  $R$  is due to the fact that the initial modelling of the Chandra AGN spectrum did not account for the starburst contamination of the AGN spectrum).

### 5.2 The nuclear starburst

The spectral modelling discussed above characterises the nuclear starburst in terms of two thermal components with temperatures of  $\sim 0.9$  and  $\sim 6.0$  keV. Very similar temperatures were observed (at least in terms of the hottest thermal components) in the nearby starburst galaxy NGC 253 by Pietsch et al. (2001), suggesting that the presence of the AGN in NGC 4945 has little impact on the thermal properties of its nuclear starburst (there is no evidence for an AGN in NGC 253). Gross features, associated with the cooler of the two starburst components, include the emission lines of Mg X/XI (1.34 keV), Si XII/XIII (1.83 keV) and S XIV/XV (2.45 keV). At higher energy, strong  $K\alpha$  line emission from helium-like iron is attributable to the hotter starburst component. High temperature plasma and associated line emission is characteristic of X-ray emission from a population of type Ib and type IIa SNR’s (e.g Behar et al. 2001). No corresponding iron edge is detected in either

of the *Chandra* or *XMM-Newton* observations. The unabsorbed luminosity of the starburst region measured from *XMM-Newton* (0.5-10 keV) is  $\sim 8 \times 10^{39}$  erg s<sup>-1</sup>. Analysis of the separate starburst and X-ray plume spectra shows that the nuclear starburst emission declines rapidly below  $\sim 1.5$  keV, probably as a result of absorbing material in the plane of the galaxy. This absorption may originate in material forming a low scale height disk and/or in material associated with the optical dust lanes of the galaxy.

### 5.3 The X-ray plume

Recent *Chandra* (Strickland et al. 2000) and *XMM-Newton* (Pietsch et al. 2001) observations have established that the outflow driven by the nuclear starburst in NGC 253 has a limb-brightened conical X-ray morphology. NGC 4945 provides a second example of such a structure. In both galaxies the limb-brightened X-ray structure correlates well with the observed the H $\alpha$  emission. A similar X-ray temperature is derived in each case. (In NGC 253 a single temperature thermal plasma with  $kT \sim 0.6$  keV fits the *Chandra* spectrum reasonably well, although the situation is more complicated in the better quality *XMM-Newton* data.) However, there are also significant differences. For example, the NGC 4945 X-ray plume displays a wider opening angle ( $\theta \sim 40^\circ$ ), and the limb brightening is most evident in the 1–2 keV band whereas in NGC 253 both the *Chandra* and *XMM-Newton* data show the limb brightened structure is apparent down to 0.5 keV. A similar physical model to that postulated by Pietsch et al. (2001) can be inferred for NGC 4945. The limb-brightened structure can be attributed to highly-excited gas with a low volume-filling factor, which is produced by an interaction between the starburst-driven wind and the dense ISM surrounding the outflow. In the case of NGC 4945, the comparative uniformity of the emission below 1 keV may be a direct observation of a mass-loaded superwind emanating from the nuclear starburst (as described by Suchkov et al. 1996). The question of why the limb-brightened component is hotter in NGC 4945 than in NGC 253 is an interesting point for future, detailed studies of this system. We derive an intrinsic luminosity of  $\sim 1.1 \times 10^{38}$  erg s<sup>-1</sup> (0.5 - 2 keV) for the superwind component from the *XMM-Newton* data.

## 6 CONCLUSIONS

We present a detailed imaging and spectroscopic analysis of the nuclear region of NGC 4945 using data from both *Chandra* and *XMM-Newton*. The main results of our study are:

- The nuclear regions display a complex X-ray morphology, including a predominantly hard source at the nuclear position (which is partially resolved in the *Chandra* data) and a soft X-ray “plume” extending to the northwest of the nucleus.
- The 0.5-10 keV emission from the nuclear source is dominated by a combination of reprocessed direct AGN continuum (in the form of neutral Compton reflection and iron K $\alpha$  line emission) and thermal emission from a nuclear starburst. The underlying AGN continuum is not observed directly in either the *Chandra* or *XMM-Newton* data, due to

heavy ( $\sim 4 \times 10^{24}$  cm<sup>-2</sup>) absorption in the line of sight to the continuum source, that cuts off the continuum below  $\sim 10$  keV.

- The neutral iron K $\alpha$  line is well fit with a narrow Gaussian profile (with an equivalent width of  $1.6 \pm 0.1$  keV), consistent with the line and the reflected continuum originating from the visible part of the torus wall. Furthermore, the best-fit value of the relative reflection parameter,  $R = 0.016$ , implies a near edge-on geometry for the torus.

- Neutral iron K $\alpha$  emission from the extended nuclear starburst region, identified with *Chandra*, implies that cool material in the environment of the starburst is also exposed to the AGN continuum flux. The thermal emission from the nuclear starburst is fit with a two temperature model, with  $kT \sim 0.9$  and  $\sim 6.9$  keV. The spectrum shows clear features associated with the two starburst components, including emission lines of Mg X/XI, Si XII/XIII and S XIV/XV from the cooler component and strong K $\alpha$  line emission from helium-like iron originating in the hotter component.

- A *Chandra* image reveals the X-ray plume to have a limb-brightened morphology in the 1–2 keV band. The plume is associated with the softest emission observed by *XMM-Newton* and is well modelled by a single temperature thermal model, with  $kT \sim 0.6$  keV. When combined, these properties suggest a physical interpretation of the plume as a mass-loaded superwind emanating from the nuclear starburst.

Finally, we note that combining the *Chandra* and *XMM-Newton* datasets has helped to mitigate the limitations of the individual observations and allowed us to carry out a much more detailed imaging and spectral study than would otherwise have been possible. This work clearly demonstrates the potential of joint *Chandra* and *XMM-Newton* analysis in characterising spatially and spectrally complex X-ray sources, such as those associated with the extended nuclear regions of nearby galaxies.

## ACKNOWLEDGMENTS

NJS gratefully acknowledges the financial support from PPARC. It is a pleasure to thank Kevin Briggs and Dick Willingale for their valuable aid with the Q software system. We also wish to thank the *XMM-Newton* and *Chandra* instrument and calibration teams for their on-going efforts to fully characterise and calibrate their respective instruments. The archival *Chandra* data were obtained from the UK mirror of the *Chandra* X-ray Center Data Archive operated by the Leicester Data Archive Service (LEDAS). This research has made extensive use of NASA’s Astrophysics Data System Abstract Service.

## REFERENCES

- Antonucci R., 1993, ARAA, 31, 473  
 Behar E., Rasmussen A. P., Griffiths R. G., Dennerl K., Audard M., Aschenbach B., Brinkman A. C., 2001, A&A, 365, L242  
 Cappi M., Bassani L., Comastri A., Guainazzi M., Maccacaro T., Malaguti G., Matt G., Palumbo G. G. C., Blanco P., Dadina M., dal Fiume D., di Cocco G., Fabian A. C., Frontera F.,

- Maiolino R., Piro L., Trifoglio M., Zhang N., 1999, *A&A*, 344, 857
- Chen Y., Huang J., 1997, *ApJL*, 479, L23
- Curran S. J., Johansson L. E. B., Bergman P., Heikkilä A., Aalto S., 2001, *A&A*, 2001, 367, 457
- Done C., Madejski G. M., Smith D. A., 1996, *ApJL*, 463, L63
- Ghisellini G., Haardt F., Matt G., 1994, *MNRAS*, 267, 743
- Greenhill L. J., Moran J. M., Herrnstein J. R., 1997, 481, L23
- Guainazzi M., Matt G., Brandt W. N., Antonelli L. A., Barr P., Bassani L., 2000, *A&A*, 356, 463
- Heckman T. M., Armus L., Miley G. K., 1990, *ApJS*, 74, 833
- Hesser J. E., Harris H. C., van den Bergh S., Harris G. L. H., 1984, *ApJ*, 276, 491
- Iwasawa K., Koyama K., Awaki H., Kunieda H., Makishima K., Tsuru T., Ohashi T., Nakai N., 1993, *ApJ*, 409, 155
- Jansen F., Lumb D., Altieri B., Clavel J., Ehle M., Erd C., Gabriel C., Guainazzi M., Gondoin P., Much R., Munoz R., Santos M., Schartel N., Texier D., Vacanti G., 2001, *A&A*, 365, L1
- Madejski G., Zycki P., Done C., Valinia A., Blanco P., Rothschild R., Turek B., 2000, *ApJL*, 535, L87
- Magdziarz P., Zdziarski A. A., 1995, *MNRAS*, 273, 837
- Matt G., Brandt W. N., Fabian A. C., 1996, *MNRAS*, 280, 823
- Mauersberger R., Henkel C., Whiteoak J.B., Chin Y.-N., Tieftrunk A.R., 1996, *A&A*, 309, 705
- Moorwood A. F. M., van der Werf P. P., Kotilainen J. K., Marconi A., Oliva E., 1996, *A&A*, 308, L1
- Ott M., Whiteoak J. B., Henkel C., Wielebinski R., 2001, *A&A*, 372, 463
- Pietsch W., Roberts T. P., Sako M., Freyberg M. J., Read A. M., Borozdin K. N., Branduardi-Raymont G., Cappi M., Ehle M., Ferrando P., Kahn S. M., Ponman T. J., Ptak A., Shirey R. E., Ward M., 2001, *A&A*, 365, L174
- Sako M., Kahn S. M., Paerels F., Liedahl D. A., 2000, *ApJL*, 543, L115
- Spoon H. W. W., Koornneef J., Moorwood A. F. M., Lutz D., Tielens A. G. G. M., 2000, *A&A*, 357, 898
- Strickland D. K., Heckman T. M., Weaver K. A., Dahlem M., 2000, *AJ*, 120, 2965
- Suchkov A. A., Berman V. G., Heckman T. M., Balsara D. S., 1996, *ApJ*, 463, 528
- Vignali C., Comastri A., 2002, *A&A*, 381, 834
- Wilson A. S., Tsvetanov Z. I., 1994, *ApJ*, 107, 1227